








Article

Biocompatibility and Degradation of Fe-Mn-5Si Alloy after Equal-Channel Angular Pressing: In Vitro and In Vivo Study

Olga Rybalchenko ¹, Natalia Anisimova ^{1,2,3,*}, Natalia Martynenko ¹, Georgy Rybalchenko ⁴,
Andrey Belyakov ⁵, Igor Shchetinin ^{1,6}, Elena Lukyanova ¹, Olga Chernogorova ¹, Arseniy Raab ⁷,
Natalia Pashintseva ⁸, Evgeny Korniyushenkov ^{2,8}, Gulalek Babayeva ^{2,9}, Darina Sokolova ^{2,9},
Mikhail Kiselevskiy ^{2,3} and Sergey Dobatkin ¹

- ¹ A.A. Baikov Institute of Metallurgy and Materials Science of the Russian Academy of Sciences, 119334 Moscow, Russia; rybalch@mail.ru (O.R.); nataliasmartynenko@gmail.com (N.M.); ingvvar@gmail.com (I.S.); helenelukyanova@gmail.com (E.L.); ochernogorova@imet.ac.ru (O.C.); dobatkin.sergey@gmail.com (S.D.)
- ² N.N. Blokhin National Medical Research Center of Oncology (N.N. Blokhin NMRCO) of the Ministry of Health of the Russian Federation, 115478 Moscow, Russia; evg-korniyushenkov@yandex.ru (E.K.); babaevagulyalek@gmail.com (G.B.); d.v.sokolova@gmail.com (D.S.); kisele@inbox.ru (M.K.)
- ³ Center for Biomedical Engineering, National University of Science and Technology “MISIS”, 119049 Moscow, Russia
- ⁴ P.N. Lebedev Physical Institute of the Russian Academy of Sciences, 119991 Moscow, Russia; rybalchenkov@lebedev.ru
- ⁵ Laboratory of Mechanical Properties of Nanostructured Materials and Superalloys, Belgorod State University, 308015 Belgorod, Russia; belyakov@bsu.edu.ru
- ⁶ Department of Physical Materials Science, National University of Science and Technology “MISIS”, 119049 Moscow, Russia
- ⁷ Institute of Physics of Advanced Materials, Ufa University of Science and Technology, 450000 Ufa, Russia; agraab@mail.ru
- ⁸ Limited Liability Company “Veterinary Oncological Scientific Center”, 115211 Moscow, Russia; pashintseva2009@yandex.ru
- ⁹ Research Institute of Molecular and Cellular Medicine, RUDN University, 117198 Moscow, Russia
- * Correspondence: n_anisimova@list.ru



Citation: Rybalchenko, O.; Anisimova, N.; Martynenko, N.; Rybalchenko, G.; Belyakov, A.; Shchetinin, I.; Lukyanova, E.; Chernogorova, O.; Raab, A.; Pashintseva, N.; et al. Biocompatibility and Degradation of Fe-Mn-5Si Alloy after Equal-Channel Angular Pressing: In Vitro and In Vivo Study. *Appl. Sci.* **2023**, *13*, 9628. <https://doi.org/10.3390/app13179628>

Academic Editor: Sasan Dadbakhsh

Received: 9 June 2023

Revised: 27 July 2023

Accepted: 23 August 2023

Published: 25 August 2023



Copyright: © 2023 by the authors. Licensee MDPI, Basel, Switzerland. This article is an open access article distributed under the terms and conditions of the Creative Commons Attribution (CC BY) license (<https://creativecommons.org/licenses/by/4.0/>).

Abstract: An attempt to improve the functional characteristics of a degradable Fe-Mn-5Si shape memory alloy by means of structure refinement by equal-channel angular pressing (ECAP) was made. In the course of ECAP, an austenitic ultrafine-grained structure was obtained. In shear bands with a thickness of 301 ± 31 nm, twins 11 ± 1 nm in size were formed. Due to the resulting structure, the tensile strength was doubled up to 1419 MPa, and the yield strength was increased up to 1352 MPa, four times higher compared with the annealed state. Dynamic indentation tests revealed a decrease in Young’s modulus by more than 2.5 times after ECAP compared to values measured in the annealed state. The results of the study of hemolytic and cytotoxic activity in vitro, as well as the local and systemic reactivity of the body of laboratory animals after implantation of the test samples indicate the biocompatibility of the alloy after ECAP. Biocompatibility, high specific strength and low modulus of elasticity open prospects for Fe-Mn-5Si alloy after ECAP to be used for the production of degradable implants that can effectively provide the fastening function in osteoreconstruction.

Keywords: Fe-Mn-Si alloys; equal-channel angular pressing; martensitic transformation; mechanical properties; biocompatibility in vitro; biocompatibility in vivo; corrosion rate

1. Introduction

Shape memory alloys (SMAs) with the ability to retain a pre-programmed shape are attractive for use in various industries, such as electronics, aircraft, automotive, etc. [1]. However, recently SMAs have become most in demand in biomedicine [2,3]. Among the materials with shape memory effect (SME) are biocompatible, bioresorbable alloys based

on Fe [4–6], such as alloys of the Fe-Mn-Si system. For the vast majority of alloys with SME, such as Ti-Ni, including those based on Fe (Fe-Pt, Fe-Ni-Co-Ti, etc.), SME occurs due to thermoelastic martensitic phase transformation. The SME in Fe-Mn-Si alloys arises as a result of stress-induced γ (fcc) \rightarrow ϵ (hcp) martensitic transformation, followed by reverse transformation on heating. The SMEs of the Fe-Mn-Si system have been constantly studied since their discovery [7–9]. This system is expected to be a promising alternative to Ti-Ni based shape memory alloys. One of its important advantages is degradation, which helps to avoid repeated surgical intervention to remove the implant, reducing the risk of side effects due to long-term use.

The effective use of Fe-based bioresorbable SME alloys in medicine requires them to meet relevant criteria. Bioresorbable materials for biomedical applications are expected to have a mechanical strength of ≥ 200 MPa with a corresponding elongation of $\geq 10\%$ [10]. It is fair to note that Fe-Mn-Si alloys with SMA have satisfactory strength and ductility, despite the fact that Si impairs the ductility of the material. For example, the Fe-30Mn-6Si alloy has a tensile strength of 453 MPa and a relative elongation of 16.5% [6]. At the same time, in Fe-Mn-Si alloys, Young's modulus is quite high compared to that of the human bones, which adversely affects the biomechanical compatibility of the implanted device and the bone [11]. However, Young's modulus can gradually decrease with increasing degradation time [12], as well as with the application of appropriate processing [13–15].

So far, several studies on the degradation and biocompatibility of Fe-based SMA have been reported [4,6,16]. In [6], the corrosion resistance of Fe-Mn-Si alloy with SME, Fe-Mn alloy and pure Fe was studied by the method of potentiodynamic polarization in the Hanks solution. It was found that the Fe-Mn-Si alloy exhibited the lowest corrosion potential and the highest corrosion current density, indicating the lowest corrosion resistance among the studied materials. In [17], this behavior was explained by the lower corrosion resistance of the austenitic and martensitic phases in the Fe-Mn-Si alloy compared to the ferrite of pure Fe. Fe-Mn-Si alloys exhibit satisfactory in vitro degradation characteristics compared to pure Fe [13,18]. The in vitro cytotoxicity test carried out in [6] demonstrated satisfactory biocompatibility of Fe-Mn-Si alloys. Studies [19,20] showed biocompatibility in vivo with the preservation of the mechanical integrity of the Fe-Mn-Si alloy. At the same time, [21] reported on the weight loss of the Fe-Mn-Si implant after a two-week implantation in the rat tibia without specifying the exact corrosion rate in vivo. However, their corrosion rate is much lower than that of the Mg-based alloys.

After confirming acceptable degradation and biocompatibility in Fe-based SMA alloys, attempts to change the composition of these alloys in order to increase the corrosion rate required for the manufacture of bioresorbable implants were made [12,22,23]. It was found that the corrosion rate of Fe-Mn-Si SMA alloys increases with increasing of Mn content: 0.48, 0.59 and 0.80 mm/year for Fe-23Mn-5Si, Fe-26Mn-5Si and Fe-30Mn-5Si alloys, respectively. Such an increase in the corrosion rate may be associated with a change in the phase composition, caused by a higher content of Mn [13]. Among other reasons for the decrease in the corrosion resistance of Fe-based alloys after alloying with Mn, are the high chemical activity of Mn, i.e., low electronegativity, a high negative value of the standard electrode potential, as well as an increased tendency to form non-metallic inclusions [24–27]. At the same time, it should be noted that a high content of manganese leads to pronounced pitting corrosion in chloride media [28]. Alloying has long been considered an effective method of controlling the corrosion rate of a metal due to its ability to either change the corrosion potential or cause micro-galvanic corrosion. Unfortunately, only a limited number of the alloying elements can cause such an effect. Therefore, other possibilities of manipulating the structure and phase composition are being studied. The concept of changing the phase composition revolves around enhancing galvanic corrosion by creating various phases with different potentials. It has been reported that this approach is also effective for bioresorbable Fe-Mn alloys [23,29]. However, in this case, there is also a limitation on the phase composition. In order to use magnetic resonance imaging (MRI)

during implantation for medical control, the material after deformation must be in an antiferromagnetic state (austenite, ϵ -martensite).

An important role in increasing the corrosion rate is played by structural defects that occur during metal processing. Violations of the regularity of the crystalline structure have a higher free energy and can become a place for the initiation of corrosion in crystalline materials [30,31]. Dislocations and grain boundaries can serve as preferred sites for the nucleation of nonequilibrium intermetallic phases [32], which can subsequently form galvanic cells with a metal matrix. In addition, it is known that the grain size affects the corrosion characteristics of the alloy. A model [33] was proposed that describes the relationship between the corrosion current density and the grain size of pure metals. Within this model for corrosion in a physiological environment, grain refinement can lead to an increase in the corrosion current density. At the same time, grain refinement leads to an increase in the density of grain boundaries. Their effect on the corrosion resistance of the alloy depends on the angles of their misorientation [34] and on the type of boundaries. Thus, in Fe-based alloys, low-angle grain boundaries lead to a decrease in susceptibility to intergranular corrosion, in contrast to high-angle grain boundaries [35]. Twins in the austenitic structure of these alloys have low energy special boundary, which increase the corrosion resistance in contrast to high-energy twin boundaries of the Mg alloys [36].

The current state of research shows great scientific interest in the direction of studying the processes of degradation and increasing the corrosion rate of alloys with SMA, including Fe-Mn-Si alloys. However, significant progress in solving the problem of increasing the rate of degradation has not yet been achieved. In this work, an attempt was made to increase the rate of degradation of the Fe-Mn-5Si alloy by refining the structure by the method of equal-channel angular pressing (ECAP), while maintaining the austenitic state. The article presents a comparative analysis of the corrosion rate of the alloy measured by various methods. Studies of the biocompatibility and degradation of Fe-Mn-Si alloys in vitro are supplemented by in vivo results, which are currently limited [19,20].

2. Materials and Methods

2.1. Alloy Preparation and Treatments

The alloy for research was melted in a Leybold Gereus L200DI furnace (Leybold, Cologne, Germany) for vacuum arc remelting from commercially pure iron, electrolytic manganese ($\approx 99.8\%$ Mn) and silicon and remelted up to 10 times. Chemical composition of the alloy was 29 wt.% Mn–5.2 wt.% Si with minor impurities: <0.01 wt.% C, <0.005 wt.% P, <0.003 wt.% S. The chemical composition was measured using wavelength dispersive X-ray fluorescence (WDXRF) spectroscopy. The major elements in the investigated samples were determined on a BRUKER S8 TIGER Series 2 WDXRF spectrometer in vacuum according to the standard method using Quantum-Express software SPECTRA^{plus} version 4.2.1. The resulting ingot was forged at a temperature of 1100°C to obtain a rod with a diameter of 16 mm. Homogenization annealing was carried out at a temperature of 1100°C for 12 h in a vacuum in quartz tubes. Annealed rods were used to make specimens for ECAP with a diameter of 10 mm and a length of 60 mm.

ECAP was carried out along route Bc (after each pass, the specimen was turned around the longitudinal axis by 90°) at a temperature of 400°C in a die with channels intersecting at an angle of 120° . Graphite lubricant was used to minimize friction with the die walls [37]. This allowed the high-strength alloy to be deformed up to four ECAP passes. The equivalent cumulative strain applied to the sample calculated for a given geometry setup with 4 ECAP passes was 3.6 [38].

2.2. Mechanical Properties

Mechanical properties were evaluated by uniaxial tensile testing using an INSTRON 3380 machine (Instron, Norwood, MA, USA) with a load of 100 kN at room temperature on miniature dog-bone tensile test specimens with a working zone length of 5.75 mm and a cross section of 2×1 mm. Vickers microhardness was measured on an Instron Wolpert

Wilson® 402 MVD microhardness tester (Instron, Norwood, MA, USA) at a load of 0.1 kgf with an indentation time of 15 s. Indentation hardness H_{IT} , indentation modulus E_{IT} and elastic recovery η_{IT} (ratio between elastic and total indentation works W_{elast}/W_{total} , where W_{elast} and W_{total} are the elastic and total works, respectively) was determined using a dynamic ultramicrohardness tester DUH-211S (Shimadzu) with a Vickers indenter at loads of 10 and 2 g in the loading–unloading mode at a loading speed of 70 mN/s according to the [39].

2.3. Microstructural Characterization and Phase Analysis

The microstructure of the samples in the coarse-grained state was studied using a scanning JSM-7001F (JEOL; Tokyo, Japan) microscope equipped with an energy-dispersive spectrometer INCA Energy 350XT (Oxford Instruments Analytical; High Wycombe, UK). The fine structure was studied by using a JEOL JEM 2100 (JEOL; Tokyo, Japan) transmission electron microscope (TEM) operating at 200 kV. The TEM foils were electro-polished using a solution of 10% perchloric acid and 90% acetic acid. The phase composition was studied on a Rigaku Ultima IV diffractometer (Rigaku; Tokyo, Japan) with $CoK\alpha$ radiation (wavelength: $\lambda = 1.7902 \text{ \AA}$).

2.4. Potentiodynamic Polarization (PDP) Measurements

The corrosion rate was evaluated from the results of electrochemical tests by the potentiodynamic polarization (PDP) method using an SP-300 potentiostat (Bio-Logic SAS; Seyssinet-Pariset, France). Corrosion studies were carried out in physiological solution with pH = 7.4 at room temperature. A flat PAR cell (Ametek Instruments, Oak Ridge, TN, USA) with a “three-electrode configuration” was used. The cell is a double-jacketed 250 mL cell for flat samples with a maximum thickness of 1 cm. Integrated into the cell Pt gauze is the counter electrode. The test samples with a minimum diameter of 3 mm and a maximum thickness of 0.6 mm were used as the working electrode. The area exposed to the solution is about 1 cm^2 . The electrode surface was polished to a mirror finish. The Ag/AgCl electrode was inserted into the bridge tube as a reference electrode. The distance between the tip of the bridge tube and the working electrode was kept constant to minimize the IR drop in the solution. Scanning was performed at a rate of 1 mV/s in the scanning range: -1000 V , $E_{OC} + 300 \text{ mV}$, where E_{OC} is the open circuit potential. The time for determining the open circuit potential was 20 min. Preliminary studies have been carried out to determine the stabilization time for open circuit potential. E_{corr} vs. time curves were measured with different exposure times in the range of 15–60 min. The PDP curves obtained after 20- and 25-min exposure time for open circuit potential were almost the same, indicating that the surface had reached a more or less stable potential. It should be noted that the Fe-Mn-Si alloy is degradable, so there is a risk of changing the surface area due to corrosion, which in turn affects the results of the experiment. Six scans were carried out for each state of the alloy. Corrosion potential, corrosion current density and corrosion rate (C_R) were obtained using EC-Lab software V11.31 (BioLogic, Seyssinet-Pariset, France) according to [40] using the following equation:

$$C_R = \frac{3.27 \cdot 10^{-3} \cdot i_{corr} \cdot EW}{\rho \cdot S}, \text{ mm/year} \quad (1)$$

where C_R is the corrosion rate (mm/y), i_{corr} —the corrosion current density extracted from the polarization curve, $\mu\text{A cm}^{-2}$; EW is the equivalent weight, g/eq; and ρ is the alloy density, g/cm^3 .

2.5. Weight Loss Test

The weight loss test was carried out in basal DMEM (Dulbecco’s Modified Eagle Medium) medium (LLC NPP “Pan Eco” Russia) according to recommendation of [41]. Test samples in the form of a quarter of a disk with a diameter of 10 mm and thickness up to 1 mm, polished to a mirror finish, were used. In each test, three samples of alloy were

used in the annealed and ECAP-treated states. The samples were immersed for 2 h in 70% ethanol, dried and immersed in 1 mL of the medium solution at 37 °C. After 1 and 14 days, the specimens were removed from the solution, rinsed with distilled water and dried at room temperature.

The corrosion rate from weight loss measurements ($C\Delta m$) was determined according to [41]:

$$C\Delta m = \frac{8.76 \cdot 10^4 (m_0 - m_\tau)}{S \cdot \rho \cdot \tau}, \text{ mm/year} \quad (2)$$

where m_0 and m_τ are the initial and the final mass of the alloys, respectively, S —the corroded surface of the alloys, cm^2 ; τ —the duration of the weight loss test, s; and ρ —the density of the alloys, g/cm^3 .

2.6. Biocompatibility In Vitro Measurements

At least 12 samples per alloy state (the initial and ECAP-treated states) were used for the biocompatibility tests. Samples were sterilized by immersion in 70% ethanol for 2 h and then dried under sterile conditions. The blood of a healthy donor stabilized with 60 IU/m heparin was used for the study. Red blood cells (RBCs) and mononuclear leukocytes (MLs) were isolated using standard methodological approaches [42].

To assess the effect of samples on hemolysis, RBCs suspended in Hank's solution were added to the alloy samples in 1 mL wells of a 24-well plate (Corning Costar, Cambridge, MA, USA) and incubated for 2.4 and 24 h at 37 °C in an atmosphere with 5% carbon dioxide. The cells incubated under the same conditions without samples of alloys were used as a control for spontaneous hemolysis. Hank's solution was used as a negative control (C_{neg}), and a sample with 100% hemolysis after adding 10 μL of Triton-X as a positive control (C_{pos}). After the incubation period, the suspension in the wells was mixed and centrifuged at 3000 rpm for 5 min, and then the absorbance (A) of the supernatant at 540 nm was measured using the multimode microplate reader Spark (Tecan, San Leandro, CA, USA). Hemolysis was calculated by the formula:

$$\text{Hemolysis} = \frac{A(\text{alloy}) - A(C_{\text{neg}})}{A(C_{\text{pos}}) - A(C_{\text{neg}})} \cdot 100, \% \quad (3)$$

To assess the cytotoxic activity, the samples were incubated in 1 mL of a complete growth medium based on RPMI-1640 supplemented with 10% fetal serum, L-glutamine and penicillin-streptomycin (all-PanEco, Moscow, Russia), with MLs at a concentration of 5×10^5 cells/mL for 24 h at 37 °C in an atmosphere with 5% carbon dioxide. MLs incubated under the same conditions without alloy sample were used as a control for spontaneous cytotoxicity. The results were taken into account by the detection of LDH release in the extracellular medium using a Lactate Dehydrogenase (LDH) Activity Assay Kit (Sigma-Aldrich, Cleveland, OH, USA) in accordance with the manufacturer's method. The result was taken into account based on the results of measuring A at 450 nm on the multimode microplate reader Spark (Tecan, San Leandro, CA, USA).

2.7. Biocompatibility In Vivo Measurements

For studies in vivo, alloy samples were implanted under the skin of Balb/c mice ($n = 10$, males, $m = 22$ g) in accordance with the requirements of [43], according to the decision of the Local Ethics Committee of the N. N. Blokhin National Medical Research Center of Oncology of the Health Ministry of Russia (#8-03, 01/03/2023). After 14 days, alloy samples were collected to study their degradation, as well as animal blood serum and subcutaneous tissue samples adjacent to implanted samples, to assess local biocompatibility and systemic toxicity.

Systemic toxicity was assessed by measuring total bilirubin, urea, creatinine and albumin in blood serum using an automatic biochemical analyzer EOS BRAVO v.200

(Hospitex Diagnostics, Moscow, Russia). The blood serum of intact Balb/c mice ($n = 5$, males, $m = 22$ g) was used as a control.

The study of tissue morphology in the area of implantation of alloys was carried out according to the standard method for preparing histological preparations stained with hematoxylin–eosin (HE), followed by examination by light microscopy.

For statistical analysis, the activity of the alloys, measured in triplicates, is presented as mean \pm standard deviation. A t -test was used to conduct a comparative analysis with controls. Differences were considered significant at $p < 0.05$.

3. Results

3.1. Metallographic Features of the Fe-Mn-5Si Alloy after Annealing

The initial structure of the Fe-Mn-5Si alloy after forging and subsequent homogenizing annealing is shown in Figure 1. It is a coarse-grained structure with an average austenite grain size of 159.5 ± 11.5 μm with annealing twins 36.5 ± 5 μm thick in it.

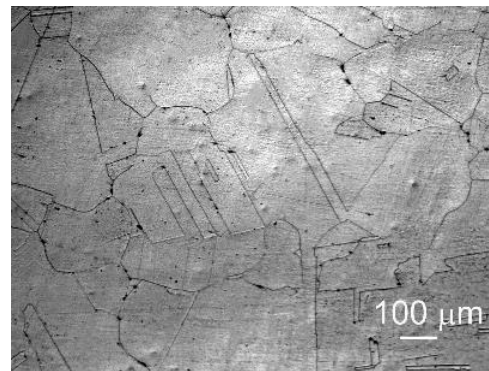


Figure 1. Optical micrographs of the Fe-Mn-5Si alloy after annealing.

3.2. X-ray Phase Analysis of the Fe-Mn-5Si Alloy after Annealing and Equal-Channel Angular Pressing

X-ray phase analysis of the alloy after annealing revealed the presence of 100% austenitic structure of the Fe-Mn-5Si alloy (Figure 2, Table 1).

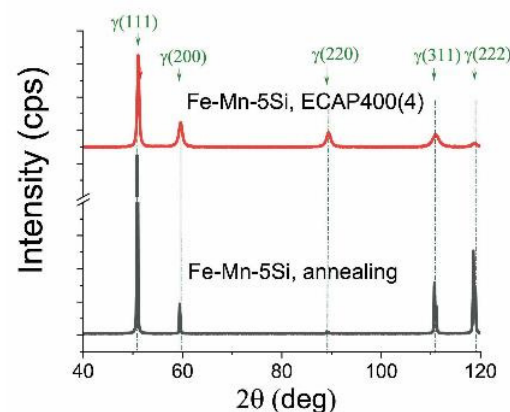


Figure 2. XRD patterns of the Fe-Mn-Si alloy after annealing and ECAP.

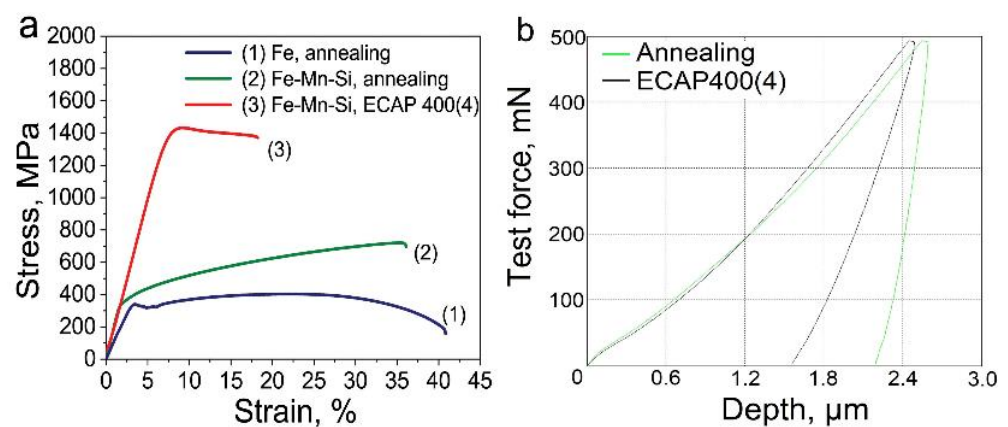
X-ray line broadening analysis showed only a microdeformation component (Table 1). The determination of the dislocation density by recalculating the microstrains obtained by a complete fitting of the diffraction profile by the Rietveld method showed that ECAP is accompanied by a 100-fold increase in the dislocation density (Table 1).

Table 1. Results of the X-ray line profile analysis of the Fe-Mn-5Si alloy after various processing methods.

Processing	Space Group	Phase	a, Å	Content, wt.%	Strain, %	Dislocation Density ρ , cm ⁻²
Annealing at 1100 °C (12 h)	225: Fm-3m	γ	3.604(1)	100	0.04(1)	6×10^9
ECAP at 400 °C, 4 passes	225: Fm-3m	γ	3.604(1)	100	0.40(1)	6×10^{11}

3.3. Mechanical Properties

The structure after ECAP significantly increased the strength characteristics of the Fe-Mn-5Si alloy samples (Figure 3a, Table 2). In this case, the tensile strength doubles to 1419 MPa compared with the state after annealing (696 MPa), and the yield strength up to 1352 MPa, 4 times higher than the yield strength of the samples after annealing (329 MPa).

**Figure 3.** Stress–strain curve of Fe-Mn-Si alloys after annealing and ECAP (a); the loading–unloading indentation curves for the samples (dynamic indentation tests) (b) at room temperature.**Table 2.** Mechanical properties of the Fe-Mn-Si alloys after annealing and ECAP.

№	Alloy and Condition	σ_{UTS}^1 , MPa	σ_{YS}^2 , MPa	ε^3 , %
1.	Fe (for comparison)	395.00 ± 4	320.5 ± 6.5	40.6 ± 1.5
2.	Fe-Mn-Si, annealing	696 ± 24	329 ± 17	33 ± 0.45
3.	Fe-Mn-Si, ECAP at 400 °C	1419 ± 14	1352 ± 6	10.7 ± 0.3

¹ ultimate tensile strength; ² yield strength; ³ total elongation.

The increase in strength after ECAP is accompanied by a decrease in ductility. The relative elongation after deformation decreases by a factor of three from 33% to 10.7%, remaining at an acceptable ECAP level (Figure 3a, Table 2).

Dynamic indentation tests based on the analysis of the dependence of the load on the indenter on the depth of its indentation into the surface of the samples after ECAP (Figure 3a, Table 2) revealed a decrease in Young's modulus by more than 2.6 times and an increase in elastic recovery by 2.5 times compared with the measured values in the state after annealing (Figure 3b, Table 3). Measurement of Vickers microhardness of ECAP-treated alloy samples showed an increase by more than 2 times compared to the annealed sample (Table 3).

Table 3. Results of dynamic indentation test of the of the Fe-Mn-5Si alloy after annealing and ECAP.

№	Alloy and Condition	H_{IT}^1 , GPa	E_{IT}^2 , GPa	η_{IT}^3 , %	HV ⁴ , GPa
1.	Annealing at 1100 °C (12 h)	3.8 ± 0.3	173.3 ± 9	14.7 ± 0.8	2.3 ± 0.8
2.	ECAP at 400 °C, 4 passes	5.0 ± 0.2	65.9 ± 2	36.7 ± 0.6	4.8 ± 1.0

¹ indentation hardness; ² indentation modulus; ³ elastic recovery; ⁴ microhardness (by 402 MVD Wolpert Wilson® tester).

3.4. Transmission Electron Microscopy (TEM) Studies of the Fe-Mn Alloys after Equal-Channel Angular Pressing

The results of mechanical property measurements testify to significant structural changes during ECAP. In samples of the Fe-Mn-5Si alloy after ECAP, the formation of an ultrafine-grained structure was revealed by transmission electron microscopy (Figure 4).

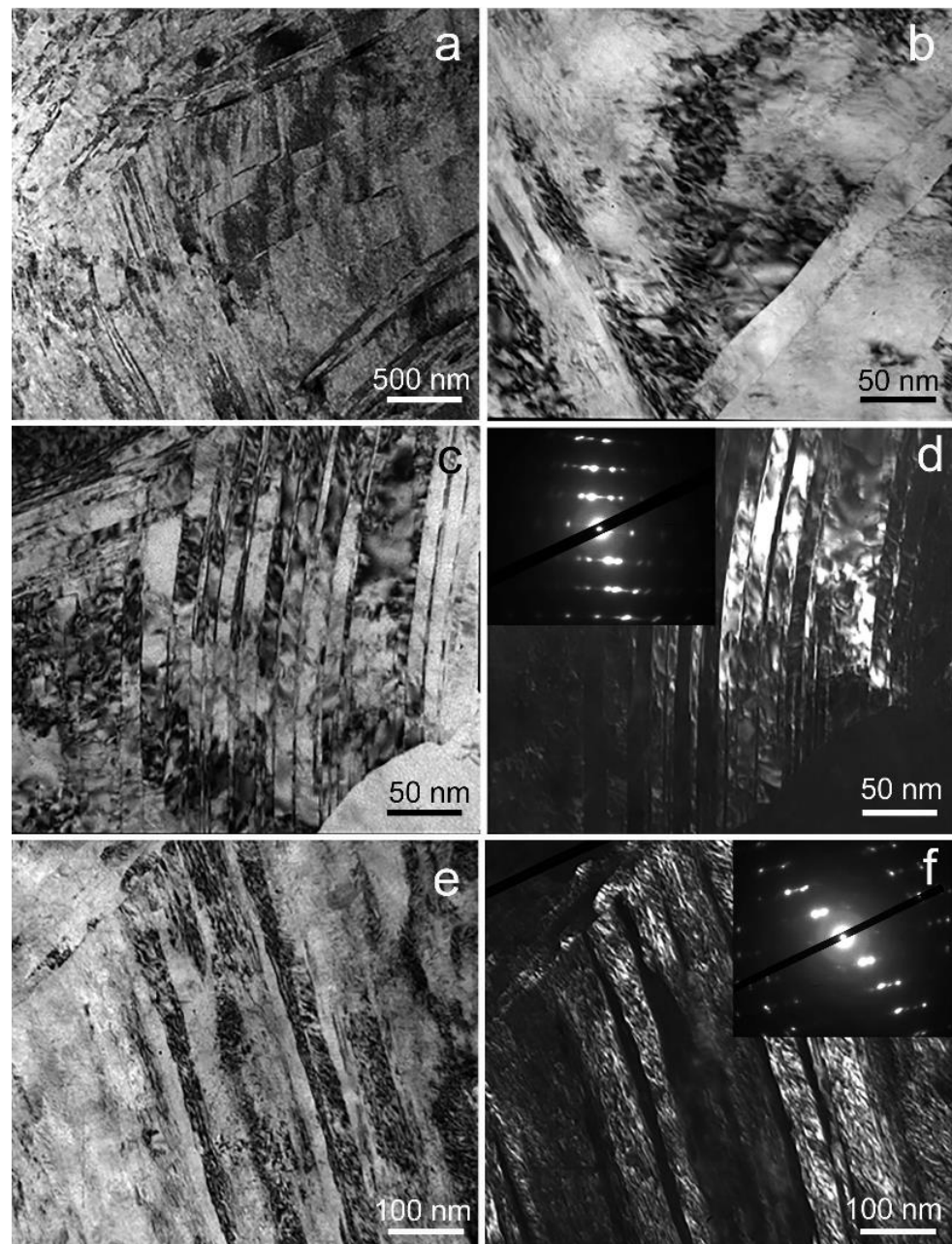


Figure 4. TEM micrographs of the microstructure of Fe-Mn-5Si alloy after ECAP: BF images (a–c,e) and DF images with SAED pattern indicating the diffraction spots corresponding to twins (d,f).

In shear bands in the range of 150–650 nm, with an average thickness of 301 ± 31 nm, twins of different sizes are formed. A typical image of the twins' microstructure is confirmed by an electron diffraction pattern from a fine structure area with a diameter of 125 nm (Figure 4c,d). Figure 4d shows a dark-field image of thin twins with a thickness of 11 ± 1 nm. Inside these twins, nanograins are formed as a result of their interaction with dislocation walls. Thicker twins with increased dislocation density are also observed (Figure 4e,f). The formation of a grain–subgrain structure also occurs when shear bands are

crossed by thick dislocation bridges and nanotwins (Figure 4b). The dislocation density inside the grains/subgrains according to TEM data exceeds $4 \times 10^{11} \text{ cm}^{-2}$.

3.5. Corrosion Rate Measurement

For the use of degradable alloys in production, one of the most important characteristics is the corrosion rate. In this work, this rate was measured by three different methods for cross-validation of the obtained results: potentiodynamic analysis, and the mass loss method in vitro and in vivo.

3.5.1. Potentiodynamic Polarization

Figure 5 shows typical potentiodynamic polarization (PDP) curves for samples of the technically pure iron and Fe-Mn-5Si alloy. The curves presented in Figure 5a show the result of single PDP measurement. The curve was chosen so that the corresponding corrosion potential was closest to the mean E_{corr} for each state. The open circuit potential (E_{oc}) and corrosion potential (E_{corr}) are almost the same. For the ECAP-treated state, the mean E_{oc} is $-802.72 \pm 6.9 \text{ mV}$ and E_{corr} is $-801.00 \pm 6 \text{ mV}$ (Table 4). The results of the potentiodynamic analysis of the Fe-Mn-5Si alloy in both the annealed state and after ECAP, as well as of the commercially pure iron, indicate a significantly lower corrosion resistance of the studied alloys compared to pure iron (Figure 5a,b). A significant shift in the corrosion potential (E_{corr}) occurs from $-539 \pm 4 \text{ mV}$ for Fe to $-778 \pm 2 \text{ mV}$ and $-801 \pm 6 \text{ mV}$ for the alloy under study in the annealed state and after ECAP, respectively (Figure 5b).

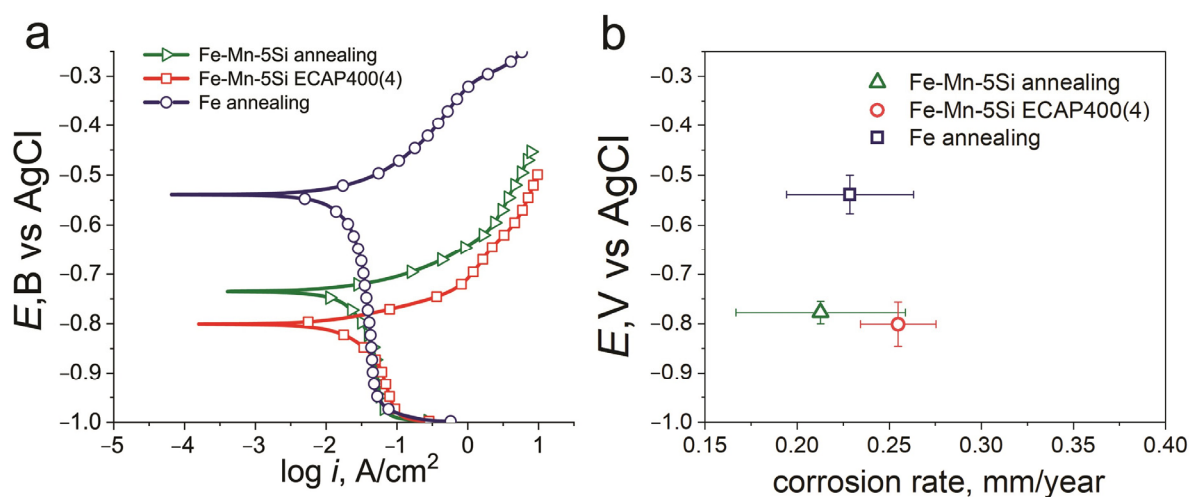


Figure 5. PDP curves in physiological saline solution at scan rate of 1 mV/s (a) and E vs. C_R (b) of the Fe-Mn-5Si alloy after annealing and ECAP in physiological solution with the pH = 7.4 at room temperature (commercially pure iron for comparison).

Table 4. Potentiodynamic polarization parameters of the Fe-Mn-5Si alloy in physiological saline solution.

	Processing	E_{corr}^1 , mV	i_{corr}^2 , $\mu\text{A}/\text{cm}^2$	C_R^3 , mm/year
Fe (for comparison)	Annealing	-539 ± 4	22.9 ± 2.4	0.24 ± 0.03
Fe-Mn-5Si	Annealing at 1100 °C (12 h)	-778 ± 2	21.5 ± 3.7	0.21 ± 0.05
	ECAP at 400 °C	-801 ± 6	21.4 ± 1.7	0.25 ± 0.02

¹ corrosion potential; ² corrosion current density; ³ corrosion rates.

The trend towards a decrease in the corrosion potential in the alloy under study can be explained by the different (by a factor of 100) dislocation density after annealing and after ECAP. However, despite the reduction in the corrosion potential, which indicates

a lower corrosion resistance of the alloy after ECAP, the corrosion rate measured by the potentiodynamic method remains virtually unchanged even compared to commercially pure iron. As mentioned above, the twin boundaries in the austenitic Fe-based alloys are the low-energy special boundary that improves corrosion resistance. The presence of twin boundaries in the structure of the Fe-Mn-5Si alloy both after annealing and after ECAP eliminates not only the imperfection of the deformed structure, but even the presence of a high manganese content in the alloy compared to commercially pure iron.

3.5.2. Degradation Rate from Mass Loss Measurements In Vivo and In Vitro

To confirm the results obtained by the potentiodynamic polarization method, the corrosion rate ($C\Delta m$) was determined by measuring the mass loss (Δm). Figure 6 shows the results of measuring $C\Delta m$ and Δm of the Fe-Mn-5Si alloy samples after annealing and after ECAP versus time of incubation or implantation. The duration of incubation in the DMEM culture medium was 1 and 14 days, and the subcutaneous implantation to mice of the Balb/c lines continued for 14 days. Studies have shown that after a day of incubation in a culture medium, the corrosion rate of the alloy in each of the states is the highest. It is 0.166 ± 0.032 mm/year for the alloy in the annealed state and 0.171 ± 0.070 mm/year after ECAP. Taking into account the measurement error, the obtained data are consistent with the results of the corrosion rate of the potentiodynamic study. Increasing the duration of the alloy incubation in the culture medium up to 14 days significantly reduces the corrosion rate to 0.018 ± 0.002 mm/year for the annealed state and to 0.028 ± 0.003 mm/year for the alloy after ECAP. These results, taking into account the measurement error, are nearly equal to the corrosion rates of samples implanted in mice for the same period, i.e., 0.013 ± 0.005 mm/year and 0.024 ± 0.008 mm/year for samples in the annealed and deformed states, respectively. In addition, measurements of $C\Delta m$ in the mass loss study confirmed that the corrosion rate of deformed samples in DMEM culture medium and after implantation in a laboratory animal for 14 days is 1.6 and 1.8 times the $C\Delta m$ of annealed samples, respectively. This is illustrated by the Δm histogram in the upper part of Figure 6.

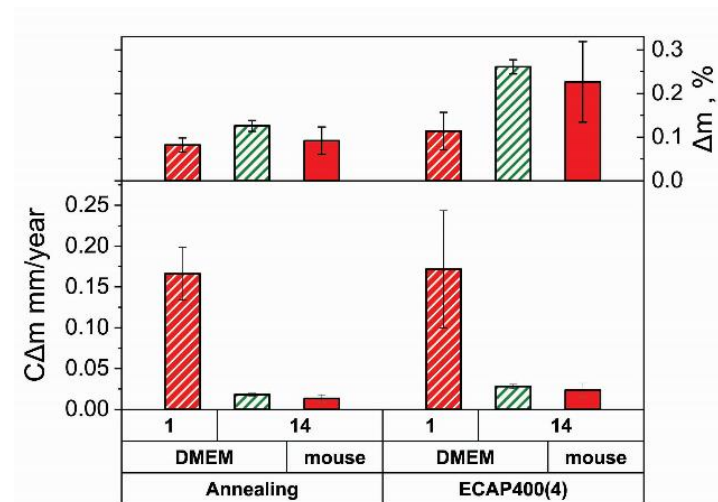


Figure 6. Corrosion rate ($C\Delta m$) and weight loss (Δm) of Fe-Mn-5Si alloy in states after annealing and ECAP vs. duration of incubation of alloy samples in DMEM and implantation in mice during 14 days.

Figure 7 shows images of the corroded surface of the samples in the annealed state (Figure 7a,b) and in the ECAP-treated state (Figure 7c,d) after their incubation in the DMEM culture medium (Figure 7a,c) and after implantation in vivo (Figure 7b,d) for 14 days.

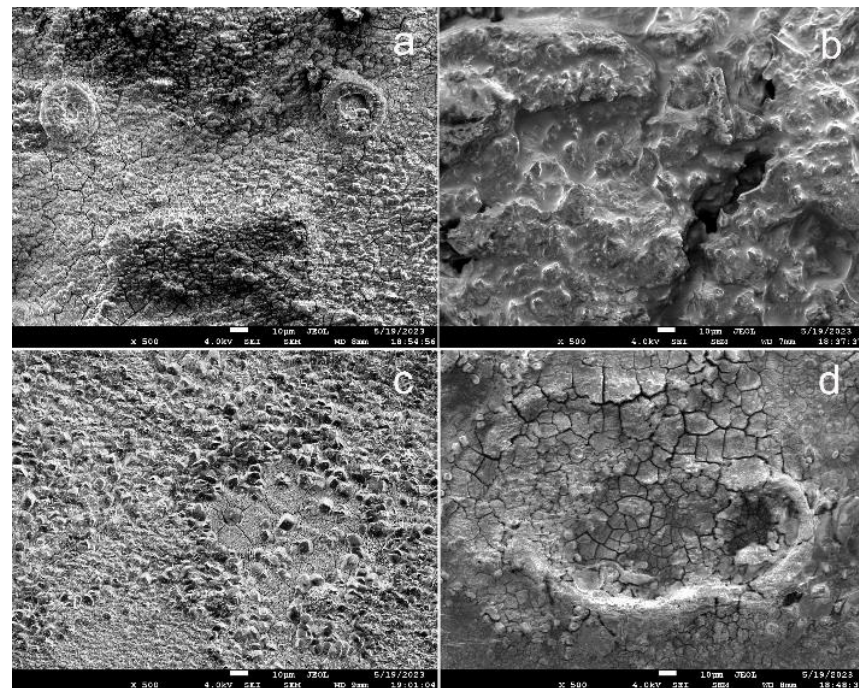


Figure 7. SEM images of surface of Fe-Mn-5Si alloy samples in the ECAP-treated state after incubation in DMEM (in vitro) (a,c) and after implantation into mouse (in vivo) (b,d) during 14 days.

A sufficiently thick layer of corrosion products was found on the surface of the samples. Visually, the appearance of corroded surfaces after incubation in vitro differed from the surface of the samples implanted in vivo. At the same time, the composition of the layer of corrosion products of annealed and deformed samples is almost identical and corresponds to that presented in the elemental mapping of ECAP-treated samples after implantation (Figure 8) and after incubation in vitro (Figure 9).

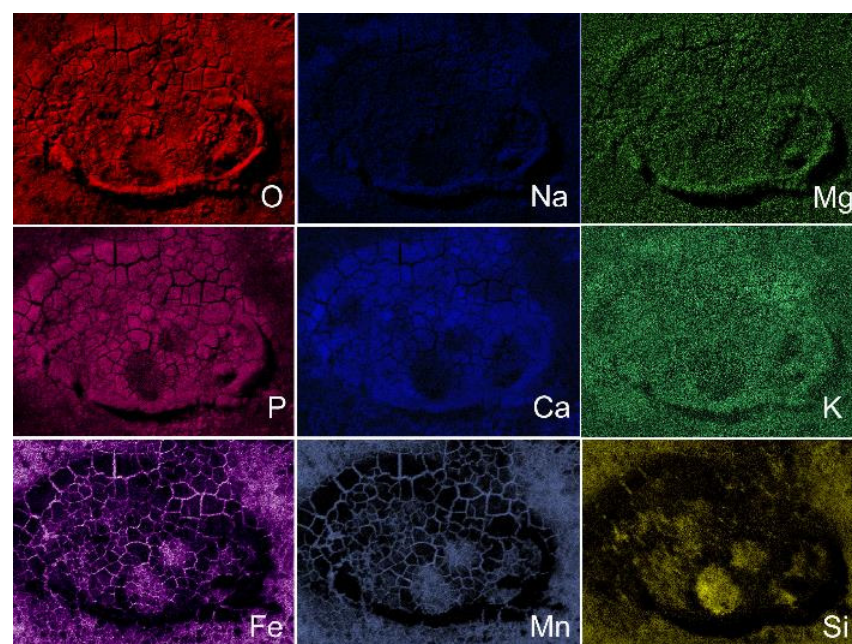


Figure 8. Elemental mapping of surface of Fe-Mn-5Si alloy samples in the ECAP-treated state after implantation in mouse (in vivo) (image in Figure 7d).

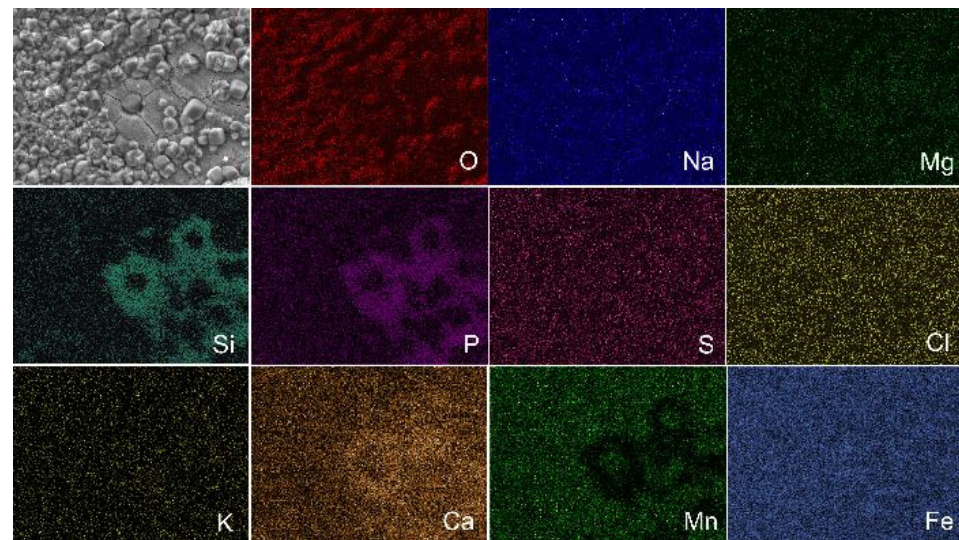


Figure 9. Elemental mapping of surface of Fe-Mn-5Si alloy samples in the ECAP-treated state after incubation in DMEM (in vitro) during 14 days.

Judging by the brightness of the P and O and Ca images on the elemental mapping (Figure 8) of the corroded surface of the samples implanted in vivo, deposits of calcium phosphate, layers of oxides, as well as pure Fe, Mn and Si on the surface of the alloy are observed, which corresponds with the observations [21]. Corrosion is slowed down due to the formation of a thick layer of corrosion products, which prevents the access of oxygen, and also due to the subsequent growth of cells on the surface of the alloy.

The elemental mapping of the corroded surface of the sample after ECAP, incubated in vitro, shows all the Ca^{2+} , Mg^{2+} , Na^+ , K^+ , Cl^- , SO_4^{2-} , PO_4^{3-} and HCO_3^- ions (Figure 9) that are part of the culture media [44]. The presence of chloride ions Cl^- led to the destruction of the protective layer of iron-based alloys, causing local pitting corrosion.

Further studies of corrosion processes showed pitting corrosion damage on the surface of the alloy both after in vitro incubation and in vivo implantation for 2 weeks (Figure 10). However, it should be noted that the signs of corrosion on the surface of the Fe-Mn-5Si alloy specimens in the ECAP-treated state were wider and less localized (Figure 10c,d), compared with the corrosion damage of the alloy samples in the annealed state (Figure 10a,b). This type of corrosion damage is more preferable for practical use, since it will not lead to premature failure of thin implantable devices. Perhaps the reason is less pronounced pitting corrosion in the absence of Cl^- ions in the medium.

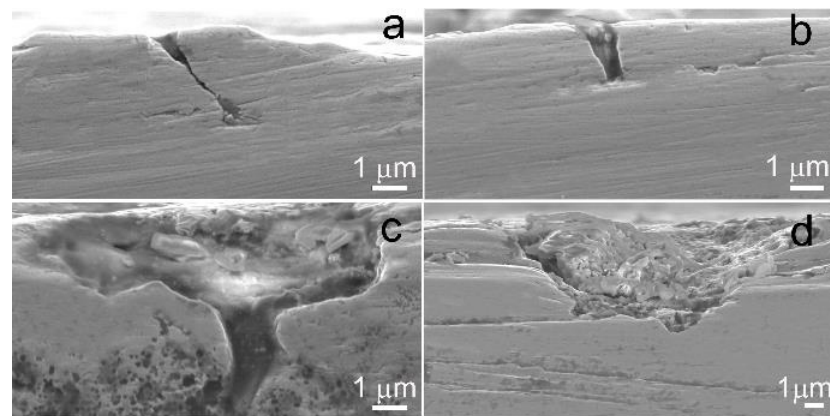


Figure 10. SEM images of the cross-section of the surface of Fe-Mn-5Si in the annealed state (a,b) and in the ECAP-treated state (c,d) after in vitro incubation (a,c) and after in vivo implantation (b,d) during 14 days.

3.6. Biocompatibility In Vitro and In Vivo

Since the Fe-Mn-5Si alloy is considered as a promising material for the development of implantable medical structures for orthopedics, it is necessary to evaluate its biocompatibility in vitro and in vivo.

3.6.1. Biocompatibility In Vitro

To assess the biocompatibility in vitro, studies of the hemolytic activity and cytotoxicity of the Fe-Mn-5Si alloy were carried out. The conducted studies showed that incubation for 2 and 4 h with samples of the Fe-29Mn-5Si alloy in the state after annealing and ECAP did not lead to a significant increase in the level of hemolysis compared with the control of spontaneous activity ($p > 0.05$) (Figure 11a). This indicates their biocompatibility in accordance with the recommendations of [45] and [46]. Even if the exposure time was extended to 24 h, the hemolysis observed in the presence of the alloy after ECAP was below 5%, which allows the use of this alloy in medical purposes.

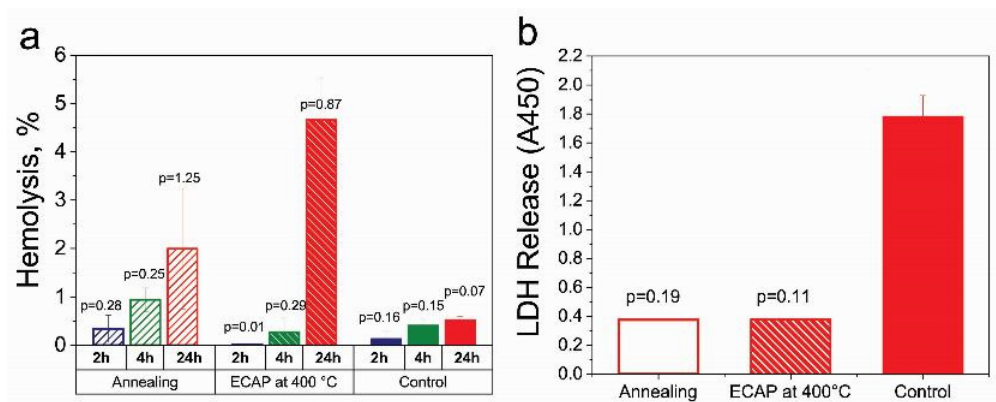


Figure 11. Biocompatibility of the Fe-Mn-5Si alloy after annealing and ECAP treatment by assessing the change in hemolysis (a) and LDH Release (b) in comparison with the control.

The cytotoxic activity of the studied alloy was assessed by measuring the activity of extracellular LDH (LDH Release), indicating cell destruction during incubation. The comparative analysis of the obtained results did not reveal signs of cytotoxicity of both types of treatments. They not only did not contribute to a significant increase in the level of extracellular LDH in comparison with the control ($p > 0.05$), but also contributed to the stabilization of the state of cell membranes. These studies of biological properties have shown that contact with alloys after annealing and ECAP does not lead to cell destruction under the described conditions. This allows us to confirm their biocompatibility in vitro.

3.6.2. Biocompatibility In Vivo

Additional investigation of the biocompatibility was made by implantation of the studied alloys under the skin of mice. In order to study the body reaction to the alloy, histological techniques for the investigation of the cell structure of the subcutaneous tissue adjacent to the implants were used. Blood biochemical parameters were assessed as markers of systemic toxicity. The vital parameters of mice with implanted specimens were compared with those of the intact animals.

A study of mouse subcutaneous tissue morphology showed that during 2 weeks after implantation, a fibrous capsule was formed around the alloy samples. The capsule was noticeably thicker around the Fe-Mn-5Si specimens after ECAP (Figure 12). The tissue of the capsule is infiltrated with a large number of fibroblasts and macrophages, which indicates the activation of cellular effectors of the destruction of the alloy and accompanies a moderate typical response to a foreign body. In the tissue surrounding the specimens, a significant amount of dilated blood vessels was detected, which probably contributed to the cell implementation, alloy bioresorption and elimination of their biocorrosion products.

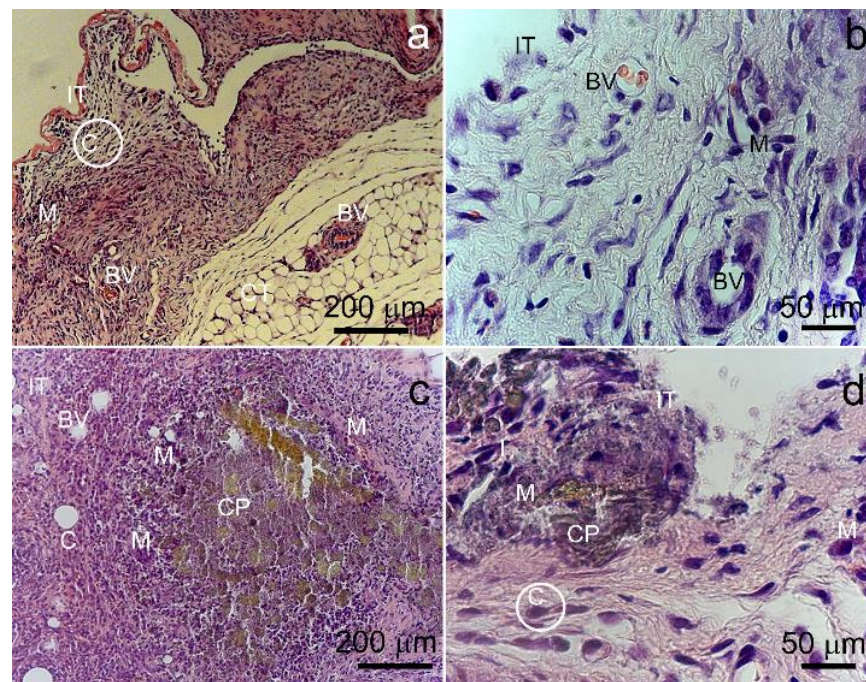


Figure 12. Mouse subcutaneous tissue adjacent to Fe-Mn-5Si alloy implants in the annealed state (a,b) and after ECAP treatment (c,d). IT—implant/tissue contact area; C—restrictive capsule; BV—blood vessels. CP—corrosion products; M—macrophages.

Accumulations of biocorrosion products were best seen around the alloy after ECAP. In general, a comparative analysis indicates that the bioresorption of the specimens after ECAP proceeded more intensively in comparison with the alloy in the annealed state, causing a more active reaction from the animal body. After implantation of alloy specimens, the skin of mice had no sign of inflammation in the area of the surgery. Therefore, the detected soft-tissue reaction was regarded as a typical process associated with the formation of granulations, aimed at healing the damage in the area of implantation. As a rule, the presence of this type of cellular infiltrate is accompanied by the formation of an early granulation tissue, and after a while, the number of cells decreases markedly.

As shown above, the accumulation of degradation products were observed in animal tissues after implantation of the studied alloy samples. It can be assumed that degradation products will enter the blood with the interstitial fluid and macrophages that phagocytized them. Degradation products accumulate in the excretory organs (liver, kidney etc.) and can induce toxic effects, which will lead to organ dysfunction and changes in biochemical markers. To study liver function, bilirubin and albumin were assessed in blood serum, and urea and creatinine were assessed for kidney function. The obtained data were compared with the results of intact animals in the control group (Table 5).

According to the results of the study of hemolytic and cytotoxic activity in vitro, as well as local and systemic reactions of laboratory animals to implants, the Fe-Mn-5Si alloy after ECAP is deemed biocompatible. Good biocompatibility, high strength and low modulus of elasticity open up excellent prospects for using the alloy in the resulting structural phase state as a material for implantable orthopedic constructions capable of providing stable osteosynthesis during the period of bone defect repair. It is worth mentioning that, due to the high strength characteristics of the Fe-Mn-5Si alloy after ECAP, it can be used to obtain miniature implants that are nevertheless capable of effectively providing the fastening function during osteoreconstructive surgery (Figure 3a, Table 2). The high specific strength of the alloy obtained by ECAP makes it possible to vary the dimensions of the implant over a wide range. This, in turn, provides additional opportunities to control the degradation time of the implant.

Table 5. Blood parameters of mice after implantation of the Fe-Mn-5Si alloy samples after annealing and after ECAP in comparison with intact animals (2 weeks after implantation).

Parameter	Intact Animals	After Implantation of Fe-Mn-5Si Alloy Samples			
		After Annealing	<i>p</i> *	After ECAP	<i>p</i> *
Bilirubin, $\mu\text{mol/L}$	6 ± 4	3 ± 2	0.55	6 ± 4	1.00
Urea, U/L	4 ± 4	6 ± 2	0.69	6 ± 4	0.75
Creatinine, U/L	79 ± 11	68 ± 14	0.58	80 ± 16	0.96
Albumin, g/L	39 ± 8	35 ± 10	0.78	37 ± 7	0.86

* samples of the Fe-Mn-5Si alloy after annealing and ECAP vs. Intact animals.

The obtained data demonstrate the absence of significant differences in biochemical parameters in animals after implantation of alloy samples with the control group ($p > 0.05$). This proves that the degradation of samples of Fe-Mn-5Si alloy after annealing and ECAP does not have a systemic toxic effect on the functioning of the main organs of the animal body and does not induce the development of acute reactive conditions by the mechanism of foreign body rejection. All of the above results allow us to confirm the *in vivo* biocompatibility of the Fe-Mn-5Si alloy.

4. Discussion

In this work, the Fe-Mn-5Si alloy, with chemical composition close to the alloys of the Fe-Mn-Si system, was studied. This system has a useful set of properties: an increased rate of degradation [13], high mechanical characteristics [6] and the maximum shape memory effect, which is ensured by the optimal content of ~5% Si and ~30% Mn in the composition of the alloy [47]. It is also important to note that the temperature of the martensitic transformation is close to the temperature of the human body [18]. In this work, we planned to use severe plastic deformation by the method of equal-channel angular pressing in order to increase the strength characteristics and the corrosion rate of this alloy [48,49]. In addition, strengthening and refinement of the structure could increase the shape memory effect of the alloy [50–52].

To obtain the initial coarse-grained state of Fe-Mn-5Si, the alloy was annealed for 12 h at a temperature of 1100 °C. During long-term annealing, a coarse-grained structure with a large number of annealing-twins was formed (Figure 1). The high density of twin boundaries in the Fe-Mn-5Si alloy and the absence of ε -martensite apparently led to a corrosion rate much lower than 0.8 mm/year, obtained in [13] for the Fe-30Mn-5Si alloy annealed at a temperature of 900 °C in an hour.

After ECAP, the austenitic state of the Fe-Mn-5Si alloy was retained due to the deformation temperature of 400 °C, which is much higher than the range of possible martensitic transformation. The austenitic state of Fe-based alloys for medical use is the most acceptable because of the possibility to use MRI as a control for the implantable device.

It should be noted that 5.12% Si decreases significantly stacking fault energy (SFE) of the alloy, since twinning in Fe-Mn alloys with a similar Mn content is not typical for high-temperature deformation [42,43]. However, the fact that twinning played a decisive role in the formation of the structure during deformation (Figure 4) resulted in the fact that the corrosion rate remained practically unchanged. The high density of defects in the crystal structure (Table 1) was compensated by an increase in corrosion resistance due to low energy boundaries in the fcc iron-based alloy.

Apparently, the resulting structural state affected the decreasing of the Young's modulus. In our work, by dynamic indentation, we obtained a decrease in Young's modulus by a factor of 2.6 from 173.3 GPa to 65.9 ± 2 GPa (Figure 3b, Table 3). This result is important in the development of alloys for bioresorbable implants, since an important factor for the use of the material is the biomechanical compatibility of the implant and bone.

It should be noted that ECAP has established itself as an effective tool for structural and phase regulation. Encouraging results have been obtained that require further research. Proper understanding of the processes of structure formation during severe plastic deformation allows one to choose the modes of thermomechanical treatment in order to obtain a set of optimal functional properties necessary for the manufacture of a biocompatible biodegradable implantable device for osteoreconstruction.

5. Conclusions

The study considers the ultrafine grained austenitic Fe-Mn-5Si alloys as a promising material for implantable devices. Structural and phase evolution during ECAP makes it possible to obtain a set of optimal functional properties necessary for the manufacture of a biocompatible degradable implantable device:

1. Long-term annealing resulted in the formation of an initial coarse-grained structure with a large number of annealing twins, which allowed the samples to withstand ECAP at 400 °C for up to four passes.
2. The highest possible strain degrees and deformation temperatures were used to achieve an ultrafine-grained structure in a fully austenitic state, which will make it possible to use MRI as an implantable device control.
3. ECAP at a temperature of 400 °C leads to the formation in the Fe-Mn-5Si alloy of an ultrafine-grained austenitic predominantly twin structure with a twin thickness of 11 ± 1 nm.
4. The structure obtained after ECAP determined a high level of strength characteristics ($\sigma_{UTS} = 1419 \pm 14$ MPa, $\sigma_{YS} = 1352 \pm 6$ MPa) with sufficiently high plasticity ($\epsilon = 4\%$) for such a state.
5. The increase in strength after ECAP is accompanied by a decrease in Young's modulus by more than 2.6 times compared with the measured values in the annealed state. This result is important for the development of alloys for bioresorbable implants. This confirms the biomechanical compatibility of the implant and bone.
6. The potentiodynamic polarization method revealed only a slight increase in the corrosion rate of the ECAP-treated alloy (0.25 ± 0.02 mm/year) compared to the alloy in the annealed state (0.21 ± 0.02 mm/year) with a significant shift in the corrosion potential of the Fe-Mn-5Si alloy in comparison with the corrosion potential of commercially pure iron.
7. The corrosion rate of the alloy in both states obtained by the mass loss measurements during incubation for a day confirmed the results of the potentiodynamic study.
8. Increasing the duration of the alloy incubation in the culture medium up to 14 days significantly reduces the corrosion rate to 0.018 ± 0.002 mm/year for the annealed state and to 0.028 ± 0.003 mm/year for the alloy after ECAP.
9. The mass loss study confirmed that the corrosion rate of deformed samples after in vitro incubation and in vivo implantation for 2 weeks is 1.6 and 1.8 times the Δm of annealed samples, respectively.
10. In vivo implantation revealed a less localized corrosion damage of the alloy sample after ECAP. Such damage is more preferable for practical use, since it will not lead to premature failure of thin implantable devices.
11. It was established that samples of the Fe-Mn-5Si alloy did not have a cytopathogenic effect on blood cells. According to the results of the study of hemolysis and cytotoxicity, the alloy was found to be biocompatible.
12. It was found that the degradation of samples of the Fe-Mn-5Si alloy after ECAP and annealing does not have a systemic toxic effect on the functioning of the main organs of the animal body. It confirms the alloy's biocompatibility in vivo.

Thus, ECAP can contribute to a significant increase in performance and reduce the weight of implanted devices, which is important for the creation of implants to replace skeletal defects, due to a significant increase in the specific strength of the Fe-Mn-5Si alloy. The high specific strength of the alloy obtained by ECAP makes it possible to

vary the dimensions of the implant over a wide range. This, in turn, provides additional opportunities to control the implant degradation time. Also, the small size of the implanted device will reduce the toxic effect of a foreign body on the human body.

Author Contributions: Conceptualization, N.A. and O.R.; methodology, N.P., M.K. and S.D.; software, G.R., A.B. and I.S.; validation, O.R., E.K. and N.M.; formal analysis, N.A. and O.R.; investigation, O.R., A.B., N.M., E.L., N.P., D.S., G.B., G.R., I.S. and O.C.; resources, A.R.; data curation, S.D. and M.K.; writing—original draft preparation, O.R. and N.A.; writing—review and editing, A.B., G.R., I.S. and N.M.; visualization, O.R. and N.A.; supervision, M.K. and S.D.; project administration, N.A.; funding acquisition, O.R. All authors have read and agreed to the published version of the manuscript.

Funding: This research was funded by the Russian Science Foundation (Grant #23-23-00096).

Institutional Review Board Statement: All manipulations with animals and cell test protocols were evaluated and approved by the Local Ethics Committee of the N. N. Blokhin National Medical Research Centre of Oncology of the Health Ministry of Russia (#8-03, 01/03/2023).

Informed Consent Statement: Not applicable.

Data Availability Statement: All data required to reproduce these experiments are presented in the article.

Acknowledgments: This research was supported by the Russian Science Foundation (Grant #23-23-00096). The study of the microstructure was carried out using research equipment of the Shared Facility Center of the P.N. Lebedev Physical Institute of the RAS Center for the Study of High-Temperature Superconductors and Other Strongly Correlated Electronic Systems.

Conflicts of Interest: The authors declare no conflict of interest.

References

1. Mohd Jani, J.; Leary, M.; Subic, A.; Gibson, M.A. A review of shape memory alloy research, applications and opportunities. *Mater. Des.* **2014**, *56*, 1078–1113. [\[CrossRef\]](#)
2. Petrini, L.; Migliavacca, F. Biomedical applications of shape memory alloys. *J. Metall.* **2011**, *2011*, 501483. [\[CrossRef\]](#)
3. Song, C. History and current situation of shape memory alloys devices for minimally invasive surgery. *Open Med. Dev. J.* **2010**, *2*, 24–31. [\[CrossRef\]](#)
4. Allenstein, U.; Ma, Y.; Arabi-Hashemi, A.; Zink, M.; Mayr, S.G. Fe-Pd based ferromagnetic shape memory actuators for medical applications: Biocompatibility, effect of surface roughness and protein coatings. *Acta Biomater.* **2013**, *9*, 5845–5853. [\[CrossRef\]](#)
5. Xu, Z.; Hodgson, M.; Cao, P. Effect of immersion in simulated body fluid on the mechanical properties and biocompatibility of sintered Fe-Mn-based alloys. *Metals* **2016**, *6*, 309. [\[CrossRef\]](#)
6. Liu, B.; Zheng, Y.F.; Ruan, L. In vitro investigation of Fe₃₀Mn₆Si shape memory alloy as potential biodegradable metallic material. *Mater. Lett.* **2011**, *65*, 540–543. [\[CrossRef\]](#)
7. Sato, A.; Chishima, E.; Soma, K.; Mori, T. Shape memory effect in $\gamma \rightleftharpoons \epsilon$ transformation in Fe-30Mn-1Si alloy single crystals. *Acta Metall.* **1982**, *30*, 1177–1183. [\[CrossRef\]](#)
8. Sato, A.; Chishima, E.; Yamaji, Y.; Mori, T. Orientation and composition dependencies of shape memory effect in Fe-Mn-Si alloys. *Acta Metall.* **1984**, *32*, 539–547. [\[CrossRef\]](#)
9. Sato, A.; Yamaji, Y.; Mori, T. Physical properties controlling shape memory effect in Fe Mn Si alloys. *Acta Metall.* **1986**, *34*, 287–294. [\[CrossRef\]](#)
10. Zheng, Y.F.; Gu, X.N.; Witte, F. Biodegradable metals. *Mater. Sci. Eng. R* **2014**, *77*, 1–34. [\[CrossRef\]](#)
11. Maruyama, T.; Kubo, H. Ferrous (Fe-Based) Shape Memory Alloys (SMAs): Properties, Processing and Applications. In *Shape Memory and Superelastic Alloys: Applications and Technologies*; Woodhead Publishing Series in Metals and Surface Engineering; Woodhead Publishing: Sawston, UK, 2011; pp. 141–159.
12. Feng, Y.P.; Blanquer, A.; Fornell, J.; Zhang, H.; Solsona, P.; Baro, M.D.; Surinach, S.; Ibanez, E.; Garcia-Lecina, E.; Wei, X.; et al. Novel Fe-Mn-Si-Pd alloys: Insights into mechanical, magnetic, corrosion resistance and biocompatibility performances. *J. Mater. Chem. B* **2016**, *4*, 6402–6412. [\[CrossRef\]](#) [\[PubMed\]](#)
13. Drevet, R.; Zhukova, Y.; Malikova, P.; Dubinskiy, S.; Korotitskiy, A.; Pustov, Y.; Prokoshkin, S. Martensitic Transformations, Mechanical and Corrosion Properties of Fe-Mn-Si Alloys for Medical Implant Applications. *Metall. Mater. Trans. A* **2018**, *49*, 1006–1013. [\[CrossRef\]](#)
14. Prokoshkin, S.; Pustov, Y.; Zhukova, Y.; Kadirov, P.; Karavaeva, M.; Prosviryakov, A.; Dubinskiy, S. Effect of Thermomechanical Treatment on Structure and Functional Fatigue Characteristics of Biodegradable Fe-30Mn-5Si (wt %) Shape Memory Alloy. *Materials* **2021**, *14*, 3327. [\[CrossRef\]](#) [\[PubMed\]](#)

15. Prokoshkin, S.; Pustov, Y.; Zhukova, Y.; Kadirov, P.; Dubinskiy, S.; Sheremetyev, V.; Karavaeva, M. Effect of Thermomechanical Treatment on Functional Properties of Biodegradable Fe-30Mn-5Si Shape Memory Alloy. *Metall. Mater. Trans. A* **2021**, *52*, 2024–2032. [\[CrossRef\]](#)
16. Huang, T.; Cheng, J.; Zheng, Y.F. In vitro degradation and biocompatibility of Fe-Pd and Fe-Pt composites fabricated by spark plasma sintering. *Mater. Sci. Eng. C* **2014**, *35*, 43–53. [\[CrossRef\]](#)
17. Lin, H.C.; Lin, K.M.; Lin, S.; Ouyang, T.M. The corrosion behavior of Fe-based shape memory alloys. *Corros. Sci.* **2002**, *44*, 2013–2026. [\[CrossRef\]](#)
18. Pustov, Y.A.; Zhukova, Y.S.; Malikova, P.E.; Prokoshkin, S.D.; Dubinskii, S.M. Structure and Corrosion-Electrochemical Behavior of Bioresorbable Alloys Based on the Fe–Mn System. *Prot. Met. Phys. Chem. Surf.* **2018**, *54*, 469–476. [\[CrossRef\]](#)
19. Fantanariu, M.; Trinca, L.C.; Solcan, C.; Trofin, A.; Strungaru, S.; Sindilar, E.V.; Plavan, G.; Stanciu, S. A new Fe–Mn–Si alloplastic biomaterial as bone grafting material: In vivo study. *Appl. Surf. Sci.* **2015**, *352*, 129–139. [\[CrossRef\]](#)
20. Trinca, L.C.; Burtan, L.; Mareci, D.; Fernandez-Perez, B.M.; Stoleriu, I.; Stanciu, T.; Stanciu, S.; Solcan, C.; Izquierdo, J.; Souto, R.M. Evaluation of in vitro corrosion resistance and in vivo osseointegration properties of a FeMnSiCa alloy as potential degradable implant biomaterial. *Mater. Sci. Eng. C* **2021**, *118*, 111436. [\[CrossRef\]](#)
21. Kraus, T.; Moszner, F.; Fischerauer, S.; Fiedler, M.; Martinelli, E.; Eichler, J.; Witte, F.; Willbold, E.; Schinhammer, M.; Meischel, M.; et al. Biodegradable Fe-based alloys for use in osteosynthesis: Outcome of an in vivo study after 52 weeks. *Acta Biomater.* **2014**, *10*, 3346–3353. [\[CrossRef\]](#)
22. Cimpoesu, N.; Sandulache, F.; Istrate, B.; Cimpoesu, R.; Zegan, G. Electrochemical behavior of biodegradable FeMnSi–MgCa alloy. *Metals* **2018**, *8*, 541. [\[CrossRef\]](#)
23. Hermawan, H.; Dube, D.; Mantovani, D. Degradable metallic biomaterials: Design and development of Fe–Mn alloys for stents. *J. Biomed. Mater. Res.* **2010**, *93*, 1–11. [\[CrossRef\]](#) [\[PubMed\]](#)
24. Zhang, Y.S.; Zhu, X.M. Electrochemical polarization and passive film analysis of austenitic Fe–Mn–Al steels in aqueous solutions. *Corros. Sci.* **1999**, *41*, 1817–1833. [\[CrossRef\]](#)
25. Della Rovere, C.A.; Alano, J.H.; Otubo, J.; Kuri, S.E. Corrosion behavior of shape memory stainless steel in acid media. *J. Alloys Compd.* **2011**, *509*, 5376–5380. [\[CrossRef\]](#)
26. Wu, X.Q.; Xu, S.; Huang, J.B.; Han, E.H.; Ke, W.; Yang, K.; Jiang, Z.H. Uniform corrosion and intergranular corrosion behavior of nickel-free and manganese alloyed high nitrogen stainless steels. *Mater. Corros.* **2008**, *59*, 676–684. [\[CrossRef\]](#)
27. Della Rovere, C.A.; Alano, J.H.; Silva, R.; Nascente, P.A.P.; Otubo, J.; Kuri, S.E. Influence of alloying elements on the corrosion properties of shape memory stainless steels. *Mater. Chem. Phys.* **2012**, *133*, 668–673. [\[CrossRef\]](#)
28. Della Rovere, C.A.; Alano, J.H.; Silva, R.; Nascente, P.A.P.; Otubo, J.; Kuri, S.E. Characterization of passive films on shape memory stainless steels. *Corros. Sci.* **2012**, *57*, 154–161. [\[CrossRef\]](#)
29. Shuai, C.; Yang, W.; Yang, Y.; Pan, H.; He, C.; Qi, F.; Xie, D.; Liang, H. Selective laser melted Fe–Mn bone scaffold: Microstructure, corrosion behavior and cell response. *Mater. Res. Express* **2020**, *7*, 015404. [\[CrossRef\]](#)
30. Dwivedi, D.; Lepkova, K.; Becker, T. Carbon steel corrosion: A review of key surface properties and characterization methods. *RSC Adv.* **2017**, *7*, 4580–4610. [\[CrossRef\]](#)
31. Toker, S.M.; Gerstein, G.; Maier, H.J.; Canadinc, D. Effects of microstructural mechanisms on the localized oxidation behavior of NiTi shape memory alloys in simulated body fluid. *J. Mater. Sci.* **2017**, *53*, 948–958. [\[CrossRef\]](#)
32. Venezuela, J.; Dargusch, M.S. Addressing the slow corrosion rate of biodegradable Fe–Mn: Current approaches and future trends. *Curr. Opin. Solid State Mater. Sci.* **2020**, *24*, 100822. [\[CrossRef\]](#)
33. Gollapudi, S. Grain size distribution effects on the corrosion behaviour of materials. *Corros. Sci.* **2012**, *62*, 90–94. [\[CrossRef\]](#)
34. Beaunier, L. Corrosion of grain boundaries: Initiation processes and testing. *J. Phys. Colloq.* **1982**, *43*, 271–282. [\[CrossRef\]](#)
35. Jiang, S.; Hewett, J.; Jones, I.P.; Connolly, B.J.; Chiu, Y.L. Effect of misorientation angle and chromium concentration on grain boundary sensitisation in an austenitic stainless steel. *Mater. Charact.* **2020**, *164*, 110343. [\[CrossRef\]](#)
36. Gerashi, E.; Alizadeh, R.; Langdon, T.G. Effect of crystallographic texture and twinning on the corrosion behavior of Mg alloys: A review. *J. Magnes. Alloy.* **2022**, *10*, 313–325. [\[CrossRef\]](#)
37. Valiev, R.Z.; Langdon, T.G. Principles of Equal-Channel Angular Pressing as a Processing Tool for Grain Refinement. *Prog. Mater. Sci.* **2006**, *51*, 881–981. [\[CrossRef\]](#)
38. Iwahashi, Y.; Wang, J.; Horita, Z.; Nemoto, M.; Langdon, T.G. Principle of equal-channel angular pressing for the processing of ultrafine-grained materials. *Scr. Mater.* **1996**, *35*, 143–146. [\[CrossRef\]](#)
39. ISO 14577-1:2015; Metallic materials—Instrumented Indentation Test for Hardness and Materials Parameters—Part 1: Test Method. International Organization for Standardization: Geneva, Switzerland, 2015.
40. ASTM G59–97/2003; Standard Test Method for Conducting Potentiodynamic Polarization Resistance Measurements. ASTM International: West Conshohocken, PA, USA, 2006.
41. ASTM G31–21; Standard Guide for Laboratory Immersion Corrosion Testing of Metals. ASTM International: West Conshohocken, PA, USA, 2004.
42. Rybalchenko, O.V.; Anisimova, N.Y.; Kiselevskiy, M.V.; Belyakov, A.N.; Tokar, A.A.; Terent'ev, V.F.; Prosvirnin, D.V.; Rybalchenko, G.V.; Raab, G.I.; Dobatkin, S.V. The influence of ultrafine-grained structure on the mechanical properties and biocompatibility of austenitic stainless steels. *J. Biomed. Mater. Res.* **2020**, *108*, 1460–1468. [\[CrossRef\]](#)

43. ISO 10993-2:2006; Biological Evaluation of Medical Devices—Part 2: Animal Welfare Requirements. International Organization for Standardization: Geneva, Switzerland, 2006.
44. Rodríguez-Hernández, C.O.; Torres-García, S.E.; Olvera-Sandoval, C.; Ramírez-Castillo, F.Y.; Muro, A.L.; Avelar-Gonzalez, F.J.; Guerrero-Barrera, A.L. Cell culture: History, development and prospects. *Int. J. Curr. Res. Acad. Rev.* **2014**, *2*, 188–200.
45. ASTM F756-08; Standard Practice for Assessment of Hemolytic Properties of Materials. ASTM International: West Conshohocken, PA, USA, 2008. [[CrossRef](#)]
46. ISO 10993-5:1999; Biological Evaluation of Medical Devices—Part 5: Tests For In Vitro Cytotoxicity. International Organization for Standardization: Geneva, Switzerland, 1999.
47. Vintaikin, E.Z.; Gulyaev, A.A.; Oralbaev, A.B.; Polyakova, N.A.; Svistunova, E.L. On the nature of the shape memory effect in Fe-Mn-Si alloys. *Metallofizika* **1991**, *13*, 43–51. (In Russian)
48. Rybalchenko, O.V.; Anisimova, N.Y.; Kiselevsky, M.V.; Rybalchenko, G.V.; Martynenko, N.S.; Bochvar, N.R.; Tabachkova, N.Y.; Shchetinin, I.V.; Shibaeva, T.V.; Konushkin, S.V.; et al. Effect of equal-channel angular pressing on structure and properties of Fe-Mn-C alloys for biomedical applications. *Mater. Today Commun.* **2022**, *30*, 103048. [[CrossRef](#)]
49. Rybalchenko, O.; Anisimova, N.; Martynenko, N.; Rybalchenko, G.; Kiselevskiy, M.; Tabachkova, N.; Shchetinin, I.; Raab, A.; Dobatkin, S. Structure Optimization of a Fe-Mn-Pd Alloy by Equal-Channel Angular Pressing for Biomedical Use. *Materials* **2023**, *16*, 45. [[CrossRef](#)] [[PubMed](#)]
50. Wei, Z.; Laizhu, J.; Ning, L.; Yuhua, W. Improvement of shape memory effect in an Fe-Mn-Si-Cr-Ni alloy fabricated by equal channel angular pressing. *J. Mater. Proc. Technol.* **2008**, *208*, 130–134. [[CrossRef](#)]
51. Druker, A.V.; Baruj, A.; Isola, L.; Fuster, V.; Malarría, J.; Bolmaro, R. Gaining flexibility in the design of microstructure, texture and shape memory properties of an Fe-Mn-Si-Cr-Ni alloy processed by ECAE and annealing. *Mater. Des.* **2016**, *107*, 153–162. [[CrossRef](#)]
52. Sato, A.; Maruyama, T.; Morishita, M.; Kumai, S.; Inoue, A. Strengthening of Fe-Mn-Si based shape memory alloys by grain size refinement. *Mater. Sci. Forum* **2000**, 327–328, 223–226. [[CrossRef](#)]

Disclaimer/Publisher's Note: The statements, opinions and data contained in all publications are solely those of the individual author(s) and contributor(s) and not of MDPI and/or the editor(s). MDPI and/or the editor(s) disclaim responsibility for any injury to people or property resulting from any ideas, methods, instructions or products referred to in the content.